

OPEN ACCESS

Sputtered Nickel Oxide Thin Films on n-Si(100)/SiO₂ Surfaces for Photo-Electrochemical Oxygen Evolution Reaction (OER): Impact of Deposition Temperature on OER Performance and on Composition before and after OER

To cite this article: M. Fingerle *et al* 2020 *J. Electrochem. Soc.* **167** 136514

View the [article online](#) for updates and enhancements.



Sputtered Nickel Oxide Thin Films on n-Si(100)/SiO₂ Surfaces for Photo-Electrochemical Oxygen Evolution Reaction (OER): Impact of Deposition Temperature on OER Performance and on Composition before and after OER

M. Fingerle,¹ S. Tengeler, W. Calvet,² W. Jaegermann,¹ and T. Mayer

TU Darmstadt Materials Science, Darmstadt 64287, Germany

Magnetron sputtered nickel oxide thin films deposited on the native oxide of crystalline n-Si(100) wafers are studied in dependence of the substrate deposition temperature (600 °C, 400 °C, 200 °C, and room temperature) using X-ray and synchrotron excited photoemission spectroscopy as well as cyclic-voltammetry under illumination. We show that the substrate temperature during nickel oxide sputtering governs the composition of the pristine NiO_x film and the OER performance. Two dedicated nickel oxide species are found with Ni²⁺ corresponding to stoichiometric NiO while Ni³⁺ indicates an oxygen rich NiO_x (x > 1) phase. With decreasing deposition temperature, the ratio of Ni³⁺/Ni²⁺ in the pristine NiO_x film increases. Information depth dependent synchrotron related photoemission spectroscopy further suggests that oxygen rich NiO_x is found on top of the surface and at the grain boundaries. The OER onset potential improves from 1.55 V to 1.1 V in correlation to an increasing Ni³⁺/Ni²⁺ ratio in the pristine NiO_x film and an increasing emission from a nickel oxyhydroxide phase (h-NiO_x) after photo-assisted cyclic-voltammetry in alkaline solution. Upon electrochemical treatment, a reconditioning process is observed with the formation of h-NiO_x that consists of Ni(OH)₂ and NiOOH, while NiO_x disappears.

© 2020 The Author(s). Published on behalf of The Electrochemical Society by IOP Publishing Limited. This is an open access article distributed under the terms of the Creative Commons Attribution 4.0 License (CC BY, <http://creativecommons.org/licenses/by/4.0/>), which permits unrestricted reuse of the work in any medium, provided the original work is properly cited. [DOI: 10.1149/1945-7111/abbcdf]



Manuscript submitted July 18, 2020; revised manuscript received September 21, 2020. Published October 12, 2020.

For nickel oxide thin films, the catalytic performance depends on structural and chemical properties which influence the electronic behaviour concerning energy distribution, density of states, as well as conductivity. The ability to split water is strongly affected by crystal orientation as shown for nickel oxide single crystals.^{1–4} In addition, defects, phase boundaries, kinks, and step-edges are considered as reaction centers.^{2,5,6} The importance of porosity and grain size of NiO_x thin films for electrochemical efficiency has been shown as well.⁷ Recently, the interface properties of nickel oxyhydroxides on semiconductor substrates in contact to the electrolyte in a photoelectrochemical cell have been studied.^{8,9} It is generally assumed that the catalytic active phase changes according to NiO_x → Ni(OH)₂ → NiOOH during electrochemical cycling in the anodic potential range. However, no defined interface experiments have been conducted so far. Therefore, we have investigated the deposition of NiO_x onto well-defined n-Si(100)/SiO_x substrates with the aim to analyze the junction properties before and after electrochemical anodization.

During magnetron sputtering the substrate temperature is one of the parameters that control the properties of the deposited material. For both, polycrystalline or amorphous thin films, defect density, phase purity, and grain size correlate with deposition temperature. Concerning most practical applications with regard to water-splitting, amorphous and defect-rich thin films often exhibit an improved performance.¹⁰ At first, the Si/NiO_x interface has been optimized with respect to the pretreatment of the Si substrate prior to the nickel oxide deposition.¹¹ Best results have been obtained with natively oxidized silicon. Referring to the experiment at hand, the next step is the optimization of the NiO_x thin film itself by varying the substrate temperature.

Defective Nickel Oxide

In general, NiO tends to be non-stoichiometric with a concentration ratio of nickel to oxygen below one. With increasing nickel deficiency, the term defective NiO_x (x > 1) is introduced to describe an oxygen rich nickel oxide phase with unclear stoichiometry. Until now, stoichiometric Ni₂O₃ could not be prepared as single-phase

material¹² which makes a clear characterization difficult.¹³ Moreover, oxygen in Ni(OH)₂ has a similar binding energy than in defective NiO_x with differences in the spectroscopic signature of both materials in XPS being very small.^{14,15} In the 1970 s, nickel oxide thin films were prepared for the first time by oxidizing metallic nickel at moderate temperatures in air. It turned out that at RT more bulk like NiO_x (x > 1) with a layer thickness of several monolayers (ml) was formed besides NiO whereas at 250 °C NiO_x (x > 1) was mainly concentrated at the surface in the thickness regime below one ml. For the respective water free process, a similar temperature dependency was obtained.^{15,16} Later, it was discovered that defective NiO_x cannot be prepared in the presence of water due to the formation of hydroxides and oxyhydroxides.¹⁷ At present, it is commonly accepted that NiO_x (x > 1) approximating the stoichiometry of Ni₂O₃ can only be formed in a water free environment at temperatures below 250 °C.

Other oxidation states: hydroxides and oxyhydroxides.—Much better characterized are the hydroxidic forms of nickel, namely nickel hydroxide Ni(OH)₂ and nickel oxyhydroxide NiOOH.^{18–21} Both species play a major role in Ni-based batteries where they are used as cathode materials. Furthermore, hydroxidic nickel exhibits strong electrocatalytic properties with a huge potential for water splitting.²² Bode et al. published a comprehensive model of the charging and discharging processes in nickel hydroxide-based batteries.²³ They identified two pseudo-polymorphous types of Ni(OH)₂ denoted with α and β, respectively. Similarly, β- and γ-NiOOH were identified as main constituents of nickel oxyhydroxide. However, a deeper discussion on the structure and on transformational processes of all these species can be found in literature.^{23–29}

Linking deposition parameters of the thin films to electronic properties is limited by experimental restrictions probing the solid/liquid interface due to the critical behavior of the liquid film under vacuum conditions. This can be overcome using ambient pressure X-ray photoelectron spectroscopy (XPS) as it has been shown e.g. for the Si/TiO₂/H₂O interface with operando XPS.³⁰ Here, we investigate the NiO_x film with photoemission before (in situ approach) and after (ex situ approach) the electrochemical treatment in the anodic regime (labeled before and after EC). The electrochemical performance during cyclic voltammetry (CV) is related to deposition temperature-controlled composition changes of the pristine material

²E-mail: wolfram.calvet@helmholtz-berlin.de

before and after the electrochemical treatment as derived from XPS. Furthermore, depth resolved NiO_x composition profiles are determined with synchrotron-based photoemission (S-XPS) experiments using a UHV based transport box (quasi in situ approach).

We find that magnetron sputtering of nickel oxide onto an n-Si/SiO₂ photo-anode leads to a mixed NiO_x phase with Ni²⁺ and Ni³⁺ valence states due to stoichiometric NiO and an oxygen rich defective NiO_x phase that is approaching "Ni₂O₃" in its stoichiometry. With decreasing deposition temperature, the "Ni₂O₃" concentration increases in the neat nickel oxide layer while in the electrochemical application the OER onset potential decreases. XPS after photo-assisted CV shows that dependent on the "Ni₂O₃" concentration in the pristine film a hydroxylated h-NiO_x phase consisting of Ni(OH)₂ and NiOOH was formed, while "Ni₂O₃" disappears. As h-NiO_x is also found in the 600 °C sample with initially no "Ni₂O₃," it is assumed that the hydroxylation proceeds also to some extent into the NiO grains.

Experimental

Sample preparation.—All experiments were performed on (001) phosphor doped n-type silicon wafers with a resistivity of 0.2 Ωcm obtained from Micro Chemicals. The samples were cleaned in an ultrasonic bath for 10 min in acetone and isopropanol followed by a short rinse with MilliQ water. The wafers are covered with a native oxide layer with a thickness of 4 ± 1 Å acting as passivation layer. In the following this kind of substrate is called n-Si/SiO_x photoanode. We found that good photoelectrochemical performance in combination with a RT deposited NiO_x thin film is achieved with this procedure (see³¹).

The as prepared substrates were dried under nitrogen flow, before being introduced within 5 min into the ultra-high vacuum (UHV) deposition and analysis system called Darmstadt Integrated System for Fundamental Research (DAISY-Fun). Thin NiO_x layers were deposited on the silicon substrates via reactive magnetron sputtering

under UHV conditions at a base pressure of 8·10⁻⁸ mbar with 19.6 sccm Ar (99.999% pure) and 0.4 sccm O₂ (99.995% pure) flow at 0.03 mbar, using a 99.99% pure nickel target at 15 W. The substrate temperature was adjusted to RT, 200 °C, 400 °C, and 600 °C with a total deposition time of 600 s resulting in 5 ± 1 nm thick NiO_x layers as deduced from the Ni2p (deposit) and Si2p (substrate) XPS core level spectra.

Sample analysis.—After the NiO_x deposition, the samples were transferred under UHV to the analysis chamber which is equipped with a SPECS Phoibos 150 analyzer and a SPECS Focus 500 X-ray source providing monochromatized AlK_α excitation at 1486.74 eV for XPS. The work function was determined by applying a bias voltage of -3 V. In addition to the lab based measurements at the DAISY-Fun system (Technical University Darmstadt), the pristine samples were also analyzed at the undulator beamline U56-2/PGM-1 at BESSY II (Helmholtz-Zentrum Berlin) using the SoLiAS (Solid/ Liquid Analysis System) end station, which is equipped with the same analyzer. By varying the excitation energy, the information depth can be tuned from extreme surface sensitive (monolayer regime) to more bulk sensitive (about 10 monolayers) conditions. The samples were transferred from the lab system to the synchrotron and vice versa using a dedicated UHV transport chamber with a small getter pump driven with a battery in order to avoid contaminations.

Electrochemistry.—After the UPS/XPS measurements, the samples were taken out of the UHV system to perform electro-chemical (EC) measurements. The sample transfer under ambient conditions was done as fast as possible to avoid unwanted contamination or damage. For this purpose, an ohmic back contact based on a gallium/indium eutectic from Alfa Aesar consisting of 99.99% pure metal [10] was prepared. Fixed on an etched copper foil, the samples were inserted into a commercially available electrochemical cell (PECC-2 from Zahner) filled with N₂ bubbled 0.1 M KOH as electrolyte. A

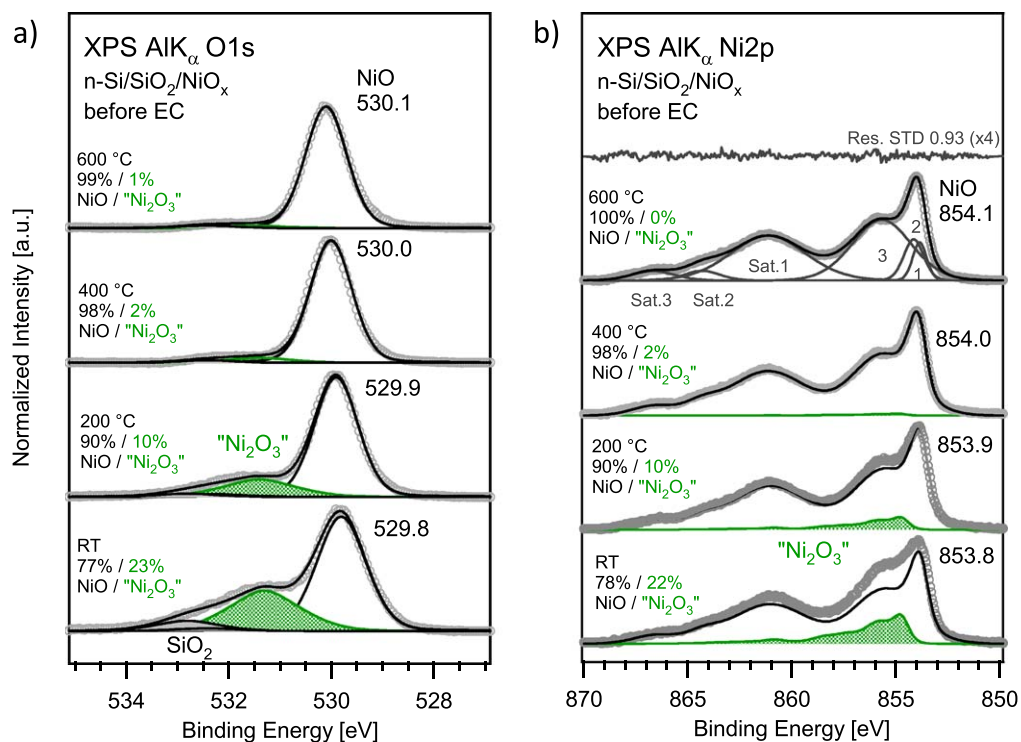


Figure 1. XPS AlK_α O1s (a) and Ni2p (b) spectra for pristine NiO_x thin films sputter-deposited on n-Si/SiO₂ photoanodes at different substrate temperatures. At 600 °C a single O1s emission is observed while at lower deposition temperature a second component (green) grows in. The Ni2p emission is most defined at 600 °C and broadens with decreasing temperature. The O and Ni spectra at 600 °C are assigned to stoichiometric NiO, a dedicated fit of the Ni2p region with the residual standard deviation (STD) is included. The binding energy of the respective NiO component (black line) is indicated and the respective "Ni₂O₃" component is shown in green as difference between the measurement (grey circle) and the energy and intensity adopted Ni2p spectrum of the 600 °C sample.

standard Ag/AgCl reference electrode was used in a three-electrode setup to control the potentials. All EC measurements were carried out using a Zennium (Zahner) potentiostat with a 625 nm (2.14 eV) LED light source operated at a power of 200 W m⁻² to excite the Si substrate. After the EC measurements, the samples were shortly rinsed with MilliQ water and subsequently transferred back into the DAISY-Fun system for post EC UPS/XPS analysis.

Spectra analysis.—The XP spectra were background subtracted using the Shirley method. A sputtered Au foil served as reference sample in order to calibrate the spectrometer by making use of the Au4f7/2 transition at 84.0 eV and the metal Fermi level located at 0 eV by definition. The XPS core level peaks were fitted using a pseudo-Voigt function with a fixed ratio of 0.2 between the Lorentzian and Gaussian distributions. As result, binding energy, line width and intensity are obtained and compared on a qualitative basis. Beyond that, intensity changes within the same binding energy region (i.e. O1s or Ni2p) were treated on a quantitative basis since cross section and kinetic energy are unchanged. A more detailed description of the used full widths at half maximum (FWHM) and the initial binding energies of the Ni2p_{3/2} and O1s core level components is given in.³² The synchrotron-based measurements were treated similarly. Excitation energy dependent cross section variations are neglected since only the O1s region with neighboring species is considered. Additional information is provided in the discussion.

Results and Discussion

Analysis of pristine NiO_x in dependence on deposition temperature.—The XPS O1s and Ni2p spectra of nickel oxide thin films sputtered at 600 °C, 400 °C, 200 °C, and RT substrate temperature on n-Si/SiO_x photoanodes are depicted in Fig. 1. In the O1s spectra (see Fig. 1a) the sample sputtered at 600 °C shows a single component indicating pure phase material, while a second component appears at higher binding energy with increasing intensity towards lower deposition temperatures. In parallel, the line shape of the Ni2p spectra in Fig. 1b is most defined at 600 °C and broadens with reduced temperatures supporting the findings above. A fit of the Ni2p spectrum based on six single components given for the 600 °C sample represents pure NiO³³ with a residual standard deviation below one. The envelope of the resulting peak structure is used for further routines as described in the following. In addition, fit parameters of the selected peaks are given in Table I to make the result comparable with other sources.^{33,34}

For 600 °C, the O1s and the Ni2p_{3/2} peak maxima are located at 530.1 eV and around 854.0 eV, respectively and fit well to stoichiometric NiO.^{33,35} Using the relative sensitivity factors of the O1s and Ni2p_{3/2} transitions as tabulated in the manual of the SPECS analyzer (with RSF = 3.6, 26.8) a value of 0.85 ± 0.15 for the [Ni]/[O] concentration ratio is obtained supporting this assumption. With decreasing deposition temperature an additional Ni2p component becomes apparent by subtracting the intensity adopted line shape of the pure NiO film deposited at 600 °C (black line) from the spectra of the films deposited at lower temperatures (grey circles). The peak

maximum of the additional low temperature component is shifted by 1.4 eV towards higher binding energy as compared to the NiO component.^{31,32} The advantage of this difference spectrum approach is that complex details of the Ni2p line shape concerning the impact of multiplet structures^{33,36} and final state effects^{37,38} can be surmounted. The [Ni]/[O] concentration ratio obtained from the fits of the according peak structures related to the second Ni2p component as shown in Figs. 1a and 1b (greenly colored) yields a value of 0.35 ± 0.15 for the RT sample which is less than the nominal stoichiometry of Ni₂O₃ but of the same magnitude. In contrast to,³⁹ the FWHM value of the second O1s peak at 531.0 eV is enlarged (see Table I) although no carbon species are involved (see Fig. 7). We assign the additional component to Ni³⁺ forming an oxygen rich defective NiO_x (x > 1) amorphous phase or a likely dispersed (nanosized) mixture of NiO/Ni₂O₃ (composite phase). Surface related effects might have an impact on the stoichiometry as well. As a consequence, besides the existing NiO phase we name the additional phase “Ni₂O₃” in short to take the stoichiometric uncertainty into account. The O1s peak ratio of the emissions of the two nickel oxide phases can be determined and compared for the different sputtering temperatures. A clear trend is visible: Starting from the sample sputtered at RT the “Ni₂O₃” concentration is between 22% and 23%. This value continuously decreases with increasing sputtering temperature. Since the nickel oxide films have a thickness of about 5 nm, photoelectrons from O1s states excited with AlK_α radiation are able to permeate the whole film as apparent in the O1s spectrum (Fig. 1a) with emission from SiO₂ still visible to a small extend.

To obtain depth profiles of the phase composition of the pristine films, the samples were also investigated at the synchrotron facility BESSY II in Berlin. By varying the excitation or photon energy in the range from hν = 580 to 1330 eV and additionally comparing to the lab-based measurements at 1486.7 eV (AlK_α), the electron escape depth λ for the O1s core level is varied from 4 to 25 Å according to the QUASES-IMPFF-TPP2M code⁴⁰ using NiO as base material. Thus, the spectra recorded at 580 eV are extremely surface sensitive, while the spectra recorded at 1486.7 eV are more bulk sensitive.

Depth profiles based on the formal “Ni₂O₃”/NiO ratios derived from the two species of the measured O1s line were determined and are plotted over λ and hν as shown in Fig. 2. In addition, best fits (solid lines) according to a basic layer model⁴¹ as depicted on the right side of Fig. 2 are included.

While for a simply layered structure where a thin “Ni₂O₃” overlayer covers the underlying NiO an exponential decay of the surface layer intensity I to the bulk intensity I_{NiO} with increasing photon energy is expected, the measured “Ni₂O₃”/NiO ratios differ significantly from this behaviour. Best fits (solid lines) according to the basic layer model (see formula on the right-hand side of Fig. 2) result in a thickness d of 0.5 Å, 0.3 Å, and 0.1 Å for the RT, 400 °C, and 600 °C prepared sample which is consistent but seems to be too small whereas I* is not physically assignable and therefore neglected. A more complex structure of “Ni₂O₃” in the nickel oxide film must be considered as shown in Fig. 2 with “Ni₂O₃” forming an overlayer and filling the NiO grain boundaries to some extent.

Table I. Spectral fitting parameters for selected peaks in Fig. 1: binding energy [eV], FWHM [eV], and percentage of total area.

Species	Region	Peak label	E _B (eV)	FWHM (eV)	% Contribution
Ni ²⁺ (600 °C)	Ni2p	1	853.9	0.8	5.8
		2	854.2	1.1	9.0
		3	855.7	3.3	39.6
		Satellite 1	861.2	4.2	37.3
		Satellite 2	864.3	2.0	3.8
		Satellite 3	866.7	2.4	4.5
Ni ²⁺ (20 °C)	O1s	NiO	529.4	1.1	76.6
Ni ³⁺ (20 °C)		“Ni ₂ O ₃ ”	531.0	1.8	23.4

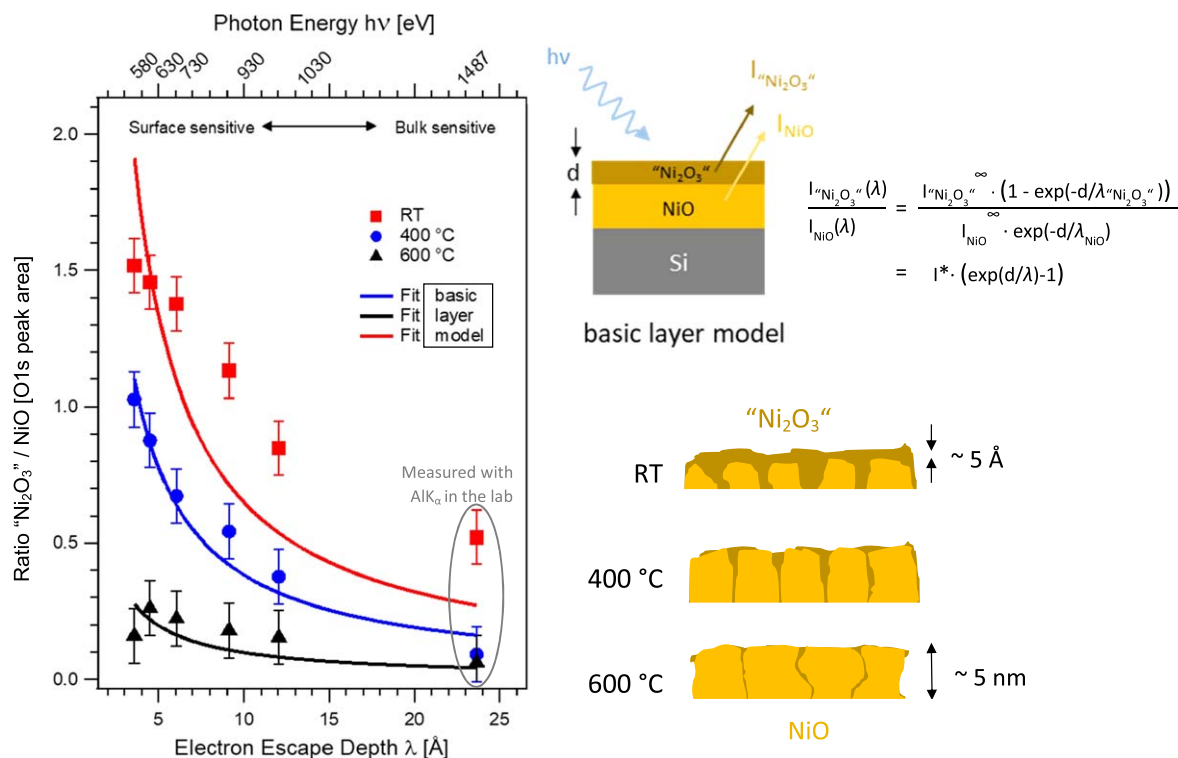


Figure 2. Excitation energy dependent “Ni₂O₃”/NiO ratios over the electron escape depth λ (photon energy) in pristine nickel oxide thin films sputtered at different substrate temperatures on n-Si/SiO_x. The evaluation is based on peak fitting of the respective O1s spectra measured at the synchrotron. In addition, lab system measured values at 1486.7 eV (AlK_α) are added. The “Ni₂O₃”/NiO ratios do not follow the exponential fits that are expected for the simple layer structure as sketched on the right-hand side. Speculative models with a more complex geometry of the “Ni₂O₃” (dark green) depth distribution in the NiO_x films are given with “Ni₂O₃” still forming the topmost layer in the RT case. In parallel, “Ni₂O₃” fills the grain boundaries between the NiO grains which become larger with increasing deposition temperatures.

Besides intermixing of both phases, it is assumed that the NiO grains are enlarged towards higher temperatures. However, further experimental techniques are required to directly measure the deposition temperature dependent grain structure of the NiO_x films.

The enhanced formation of “Ni₂O₃” under RT conditions is beneficial for the electrochemical performance as it will be shown later in this work. While the oxygen evolution reaction (OER) under illumination mainly takes place at the solid/liquid interface, the n-Si/SiO_x/NiO_x interface itself also has a strong impact on energetics and charge transfer. It must be considered as well when optimizing the whole device. In Fig. 3 various XP spectra of the RT, 400 °C, and 600 °C prepared samples before EC are shown that are related to the energy level alignment of the n-Si/SiO_x/NiO_x anodes in the dark. Fundamental parameters such as work function, valence band maximum, and band bending show distinct correlations with temperature.

As it can be clearly seen in Fig. 3a, the work function jumps down in one step from $\Phi = 5.5$ eV for the RT prepared sample to $\Phi = 4.7$ eV for the samples prepared at higher temperatures following the same trend of the Ni₂O₃ concentration as determined with XPS. In accordance to the presumed model of a dedicated “Ni₂O₃” layer on top of the RT prepared NiO_x film, the value of $\Phi = 5.5$ eV is assigned to trivalent nickel while $\Phi = 4.7$ eV stands for bivalent nickel oxide. This further confirms the image of a completely closed “Ni₂O₃” overlayer in the RT case since the spectral features of the NiO secondary electron cut off as visible for higher temperatures are fully suppressed. It is assumed that for higher preparation temperatures most parts of the NiO grains are forming the topmost layer thus ruling the work function then. In this case patches of NiO and “Ni₂O₃” coexist on top of the NiO_x film with NiO related areas getting larger for elevated preparation temperatures (see Fig. 2). In parallel, the valence band maxima of the NiO_x films steadily shift to higher binding energies with increasing temperature. Values of

VB_{max} = 0.6 (RT), 0.8 (400 °C), and 0.9 eV (600 °C) are obtained from the XPS measurements shown in Fig. 3c. The deviation of the energetic position of the Si2p peaks from the expected one in n-doped bulk silicon accounts for a band bending at the n-Si/SiO₂ interface. As expected, it is directed upwards due to pronounced Fermi-level pinning that is induced by oxygen related interfacial gap-states located 0.6 eV above the valence band edge.⁴² Following the shift of the Si2p peaks in Fig. 3b the band bending in Si increases roughly from 0.4 eV, to 0.45 eV, and 0.5 eV for the RT, 400 °C, and 600 °C sample, respectively. By making use of fundamental silicon related parameters like band gap E_G = 1.12 eV, electron affinity χ = 4.05 eV and conduction band minimum E_C – E_F ≈ 0.1 eV which on its part is dependent on dopant species and concentration level and which both are known, the discontinuity of the vacuum level E_{Vac} in the interface region and thus the involved dipole drop over the whole n-Si/SiO_x/NiO_x structure was calculated. A pronounced change is observed when going from the RT to the high temperature samples with δ = 0.95 (RT), 0.1 (400 °C), and 0.05 eV (600 °C), respectively. Energy diagrams of the layered device structure deduced from the obtained results are given in Fig. 4.

As it can be clearly seen in Fig. 4, the silicon valence band edge is well aligned with the topmost NiO_x valence states for the RT prepared sample. There is almost no offset visible compared to the high temperature preparations at 400 °C and 600 °C. While the band diagram itself does not allow for the determination of the current performance like fill factor or maximum power point, VB_{max} gives a good estimate of the achievable photovoltage U_{ph} as upper limit. Moreover, the band alignment depicted in Fig. 4 only represents the energetic situation under open circuit conditions in the dark neglecting the solid/liquid interface. The total performance of an integrated water splitting device under operation combines the IE behavior of the buried junction with the catalytic performance of the topmost layer in contact to the electrolyte. Therefore, cyclic

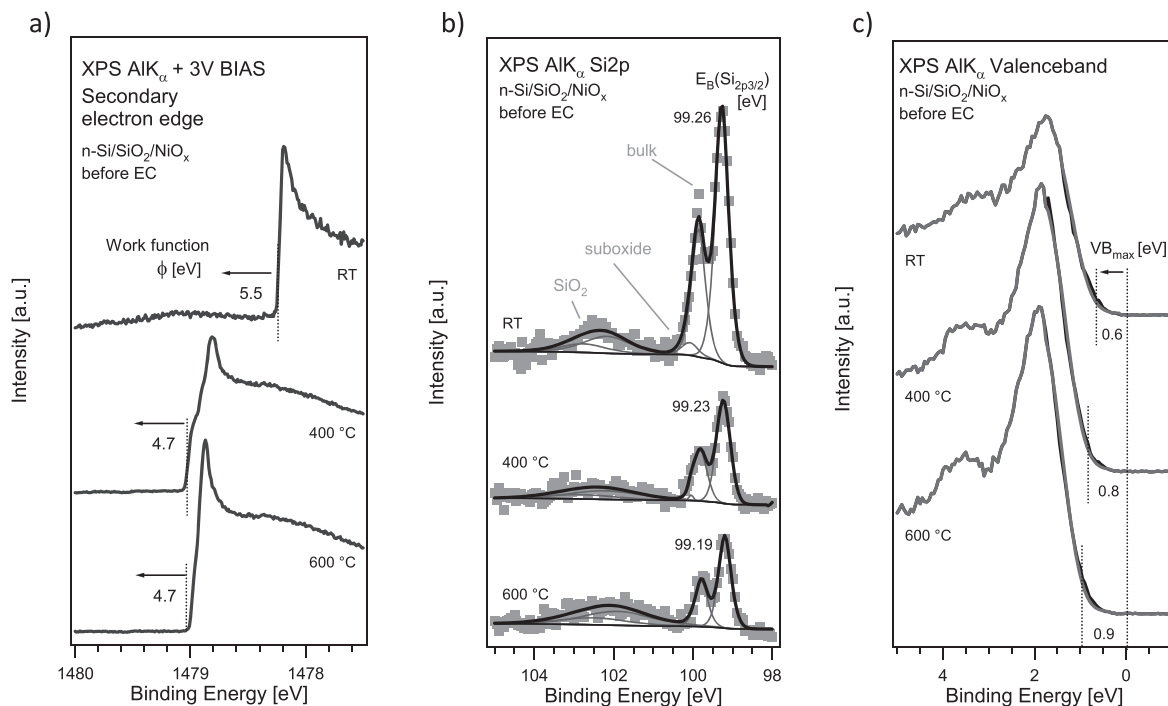


Figure 3. In situ measured XP spectra of differently prepared NiO_x films before EC: (a) Secondary electron cut off edges measured with a bias voltage of 3 V to determine the work function, (b) $\text{Si}2p$ core level emissions from the substrate measured through the thin NiO_x films with according fits to estimate the energetic alignment of the inner $n\text{-Si/SiO}_x/\text{NiO}_x$ contact with respect to the Fermi level, and (c) valence band regions with onset and according fit to obtain the valence band maximum VB_{max} (more details are given in the text).

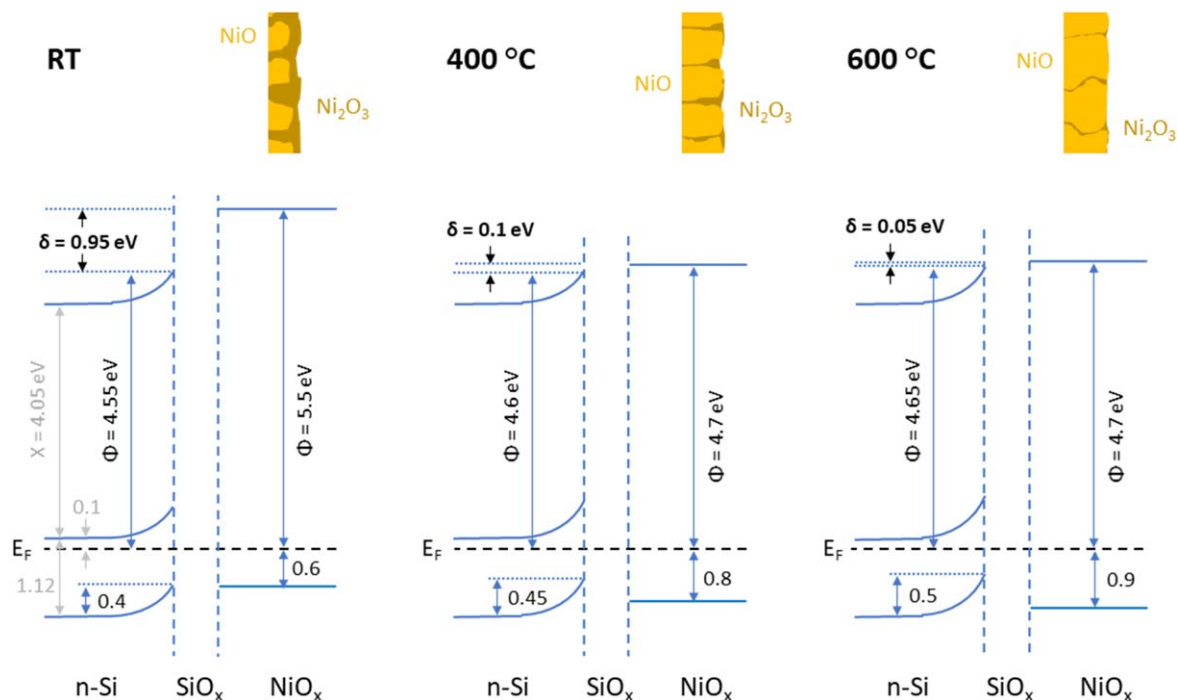


Figure 4. Energy level alignment of the $n\text{-Si/SiO}_2/\text{NiO}_x$ photoanodes sputtered at different temperatures. In addition, sketches of possible thin film NiO_x configurations are inserted as already shown in Fig. 2. The grey colored labels are referred to the fundamental values of n -doped silicon whereas the other ones are derived from XPS measurements. The dipoles δ are calculated from the drop in the vacuum level E_{vac} in the interface region.

voltammetry (CV) under illumination was applied to prove the IE performance of the whole $n\text{-Si/SiO}_x/\text{NiO}_x$ device structure in contact to the electrolyte.

The pristine samples were cycled under illumination in 0.1 M KOH. In Fig. 5 CV curves of the NiO_x films on $n\text{-Si/SiO}_x$ under illumination are depicted for the OER reaction dependent on the

deposition temperature. The OER onset potential clearly decreases from 1.55 to 1.1 V with lower temperatures, i.e. with increasing “ Ni_2O_3 ” concentration in the pristine films whereas the photocurrent density at high potentials is limited by the light intensity. In addition, the first CV cycles show a distinct spread indicating a conditioning process as stated elsewhere,⁴³ which is most

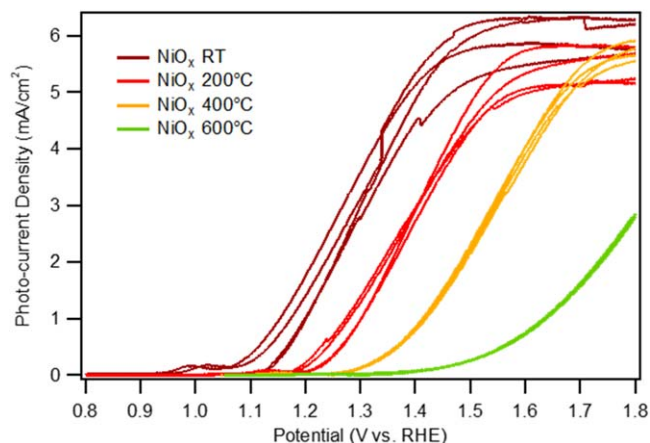


Figure 5. Comparison of the photo-current cyclic voltammetry behavior of the n-Si/SiO_x photoanodes coated with thin NiO_x films sputtered at different substrate temperatures.

pronounced for the RT prepared photo-anode. In order to analyze this conditioning process, the samples were investigated again after photo-CV by XPS (Fig. 6).

After the electrochemical characterization, the samples have been investigated again with XPS using AlK_α radiation. In Fig. 6b, the Ni2p spectra after EC are shown for different deposition temperatures. An additional peak structure referred to hydroxylated nickel oxide h-NiO_x is found by subtracting the NiO line shape as given by the pristine film grown at 600 °C with a nearly pure NiO composition that was fitted in intensity to minimize the respective NiO peak at 853.9 eV.

The O1s spectra in Fig. 6a exhibit two main peaks located at 529.4 eV and 531.3 eV that can be assigned to NiO and Ni(OH)₂ in accordance to.⁴⁴ In addition, emissions related to NiOOH (O₂⁻) and NiOOH (OH⁻) can be fitted next to the Ni(OH)₂ peak assuming

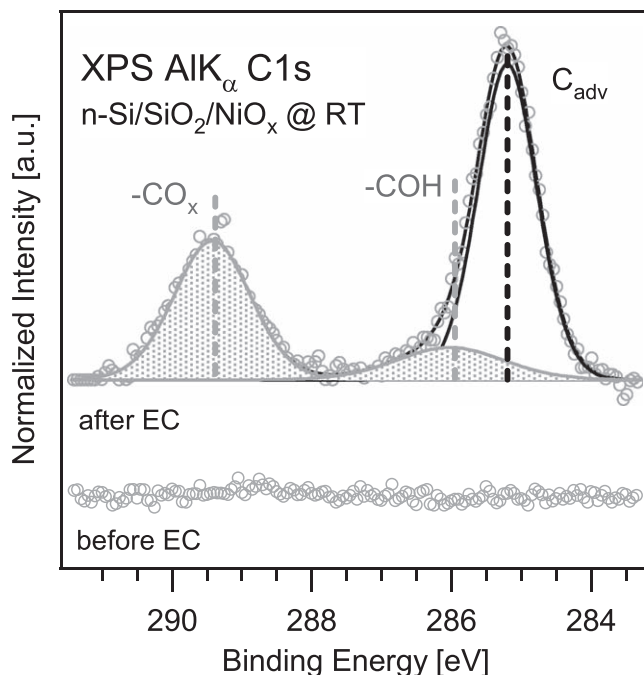


Figure 7. XP C1s spectra of the NiO_x film on n-Si/SiO₂ prepared at 20 °C before and after EC.

equal intensities.³¹ The obtained binding energy values of about 531.0 eV and 532.0 eV that are slightly varying with the preparation temperature of the NiO_x films are different from the values claimed in.⁴⁴ but they are in the same region. Furthermore, ex situ performed electrochemistry leads to an additional carbon contamination as shown in Fig. 7 for the 20 °C sample. Before EC there is nearly no carbon visible whereas after EC distinct emissions in the C1s region

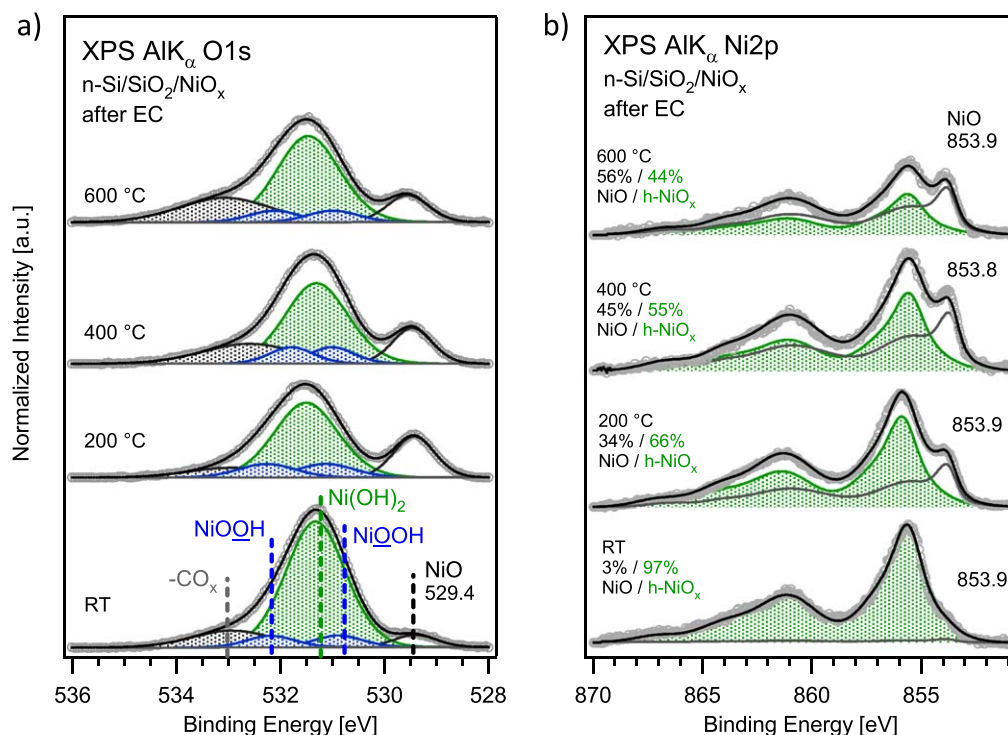


Figure 6. Post photo-CV XP O1s (a) and Ni2p (b) spectra for NiO_x films on n-Si/SiO₂ as a function of the deposition temperature. The Ni2p emission is decomposed into a NiO and a h-NiO_x (green area) component by subtracting the NiO line shape of pure NiO of the pristine 600 °C sample. The intensity of the subtracted NiO emission is fitted to minimize the NiO peak at 853.9 eV. The O1s emission reveals that h-NiO_x is mainly composed of Ni(OH)₂ besides NiOOH and NiOOH.

appear at 285.2 eV, 286.0 eV, and 289.4 eV attributed to adventitious C (C_{adv}) and to functional groups like $-\text{COH}$ or $-\text{CO}_x$.⁴⁴ This behaviour is similar for the other samples (200 °C, 400 °C, and 600 °C) and thus not shown here. Consequently, the broad line at 532.9 eV in the O1s spectra of Fig. 6a is assigned to oxidized carbon (see Table II). Although it is known that the valency of carbon in CO_x affects the quantitative analysis,⁴⁵ this aspect is less regarded as the result of the O1s peak fitting is not very straightforward. Correlations with the preparation temperature of the NiO_x films are not consistent, especially for the samples prepared at higher temperatures. At first glance, the NiO peak intensities in the O1s spectra first increase from 20 °C to 200 °C before they are decreasing towards 600 °C while the Ni(OH)_2 peak intensities are fluctuating. On closer inspection, the relative NiO concentration is lowest for the 20 °C sample (5%) compared to the other samples (between 11% and 19%). The same applies for the NiO/ Ni(OH)_2 intensity ratio that is much lower for the RT sample (0.07) than for the samples prepared at higher temperatures (between 0.21 and 0.35). This is in accordance to the relative Ni(OH)_2 concentration that is highest for the RT sample (71%) compared to the other samples (between 52% and 54%). Even an assumed error of 10% in determining the peak intensity by fitting does not change this significance. Moreover, the $\text{Ni(OH)}_2/\text{NiOOH}$ intensity ratio is about twice as high for the RT sample compared to the other samples (here NiOOH is equal to $\text{NiOOH} + \text{NiOOH}$). Altogether this means that for the RT sample the relative Ni(OH)_2 concentration is highest whereas the ones for NiO and NiOOH both are lowest. However, the volatile behaviour of the peak intensities for the samples prepared at higher temperatures cannot be explained in terms of the preparation conditions. This may be attributed to the ex situ transfer of the samples back to the XPS analysis system after EC under ambient conditions leading to an additional water and carbon related contamination or to an unknown electrochemical mechanism that changes the NiO_x film in contact with aqueous KOH depending on the initial state. Obviously, hydroxides and oxyhydroxides forming the outmost reactive layer under OER conditions are mostly involved. The fact that in Fig. 6a Ni(OH)_2 and NiOOH constituents are both present leads to the terminus hydroxylated nickel oxide h-NiO_x using one line shape (green shaded) that combines both species as shown in Fig. 6b. The attempt to resolve both components in the Ni2p spectra as described in Biesinger et al.³⁴ was not successful due to the complexity of the system consisting of NiO, Ni(OH)_2 , and NiOOH related species then.

Besides carbon and water related contamination that occurs upon the electrochemical treatment, the impact of residual iron on the formation of the nickel hydroxide films in the electrolyte has been discussed in the past. It was found that traces of iron in the KOH electrolyte (on sub-ppm level) increase the activity of the initial NiO_x films by a factor of more than 30.⁴⁶ There is clear evidence that this improvement is due to the incorporation of Fe into the NiO_x film forming active sites. This is in accordance to previous work with $\text{Ni}_{0.9}\text{Fe}_{0.1}\text{O}_x$ being reported to be the most active OER electrocatalyst among various transition metal oxides based on Co, Fe, Ni, Ir, and Mn.⁴³ Obviously, small amounts of Fe in NiO_x are sufficient to improve the OER performance due to the formation of layered $\text{Ni}_{0.9}\text{Fe}_{0.1}\text{OOH}$ oxyhydroxides with nearly every Ni atom being

electrochemically active. Furthermore, the effect of iron on phase transition or formation as well as possible doping of the host material during electrochemistry is widely discussed^{47–49} and confirms that Fe even in low concentrations can not be neglected. However, the shift of the OER onset potential in the cyclic voltammograms of pure Ni(OH)_2 layers using Fe-free and Fe contaminated KOH is roughly 0.13 V⁴⁶ (as derived from the graph) and cannot explain the 0.45 V shift we measured between RT and 600 °C using the same, possibly Fe contaminated KOH electrolyte. This means, beneath residual Fe in the KOH electrolyte which is assumed to shift all curves in Fig. 5 in the same manner by about 130 mV towards lower potentials, there must be another reason for the occurrence of the different shifts depending on the preparation temperature of the initial NiO_x films. Since our material consists of at least two phases, namely NiO and “ Ni_2O_3 ” we assume that besides structural and morphological aspects, the ratio of two species in the compound and thus the amount of defective “ Ni_2O_3 ” is responsible for the improved OER performance shifting the onset potential accordingly to the left. The improved incorporation of Fe in “ Ni_2O_3 ” cannot be ruled out and should be taken into account in the future as this would affect the OER performance as well.

Concerning the XPS measurements of the Ni2p region in Fig. 6b, the $\text{h-NiO}_x/\text{NiO}$ emission ratio clearly increases with decreasing NiO_x deposition temperature, as the “ Ni_2O_3 ”/ NiO emission ratio in the pristine samples did. Since the $\text{h-NiO}_x/\text{NiO}$ ratio seems to be larger than the “ Ni_2O_3 ”/ NiO ratio was in the pristine samples, we conclude that not only “ Ni_2O_3 ” reacts to h-NiO_x , but the hydroxylation reaction also involves stoichiometric NiO and proceeds to some extent into the NiO grains. A good fitting of the O1s spectra in Fig. 6a is achieved without any “ Ni_2O_3 ” component that would be expected about 0.4 eV lower binding energy than Ni(OH)_2 . We assume that “ Ni_2O_3 ” is fully consumed in the hydroxylation process.

Dealing with chemical reactions that may occur on the pristine NiO_x film assuming a mixture of NiO and stoichiometric Ni_2O_3 at the surface and at the grain boundaries the following reaction paths of a stoichiometric transformation under OER conditions in alkaline aqueous solution are considered: (I) $\text{Ni}_2\text{O}_3 + \text{H}_2\text{O} \rightarrow 2\text{NiOOH}$ only with Ni_2O_3 , (II) $x\text{Ni}_2\text{O}_3 + y\text{NiO} + (y+x)\text{H}_2\text{O} \rightarrow y\text{Ni(OH)}_2 + 2x\text{NiOOH}$ with Ni_2O_3 and NiO (x, y are positive integers), and (III) $\text{Ni}_2\text{O}_3 + \text{NiO} + 3\text{H}_2\text{O} \leftrightarrow 3\text{Ni(OH)}_2 + \frac{1}{2}\text{O}_2$ also with Ni_2O_3 and NiO. While reactions (I) and (II) take place without any oxygen evolution, reaction (III) is conducted by an additional oxygen evolution competing with the OER. Apparently, the availability of Ni_2O_3 in the NiO grain boundaries of the pristine NiO_x film is advantageous with respect to the formation of OER beneficial h-NiO_x which is composed of NiOOH and Ni(OH)_2 and which could be clearly measured with XPS. Similar results are found in XPS recorded valence band spectra of the differently prepared n-Si/ $\text{SiO}_2/\text{NiO}_x$ photoanodes after the EC treatment as shown in Fig. 8.

In Fig. 8a XP spectra of the nickel oxide thin films in the valence band region after EC are presented. In addition, the valence band spectrum of the RT prepared sample before EC is shown. All spectra are normalized to the Ni3d shoulder located at about 1.7 eV. Corresponding to the deposition temperature dependent increase in h-NiO_x which mainly consists of Ni(OH)_2 and NiOOH as displayed

Table II. Spectral fitting parameters for selected peaks in Fig. 6: binding energy [eV], FWHM [eV], and percentage of total area.

Species	Region	Peak label	E_B (eV)	FWHM (eV)	% Contribution
Ni^{2+} (20 °C)	O1s	NiO	529.4	0.95	4.8
		NiOOH	530.9	1.09	5.4
		Ni(OH)_2	531.3	1.35	71.6
		NiOOH	532.2	1.09	5.4
		CO_x	532.9	1.79	12.8
Ni^{2+} (600 °C)	Ni2p	NiO	853.9	1.0	56.2
		h-NiO_x	855.7	1.0	43.8

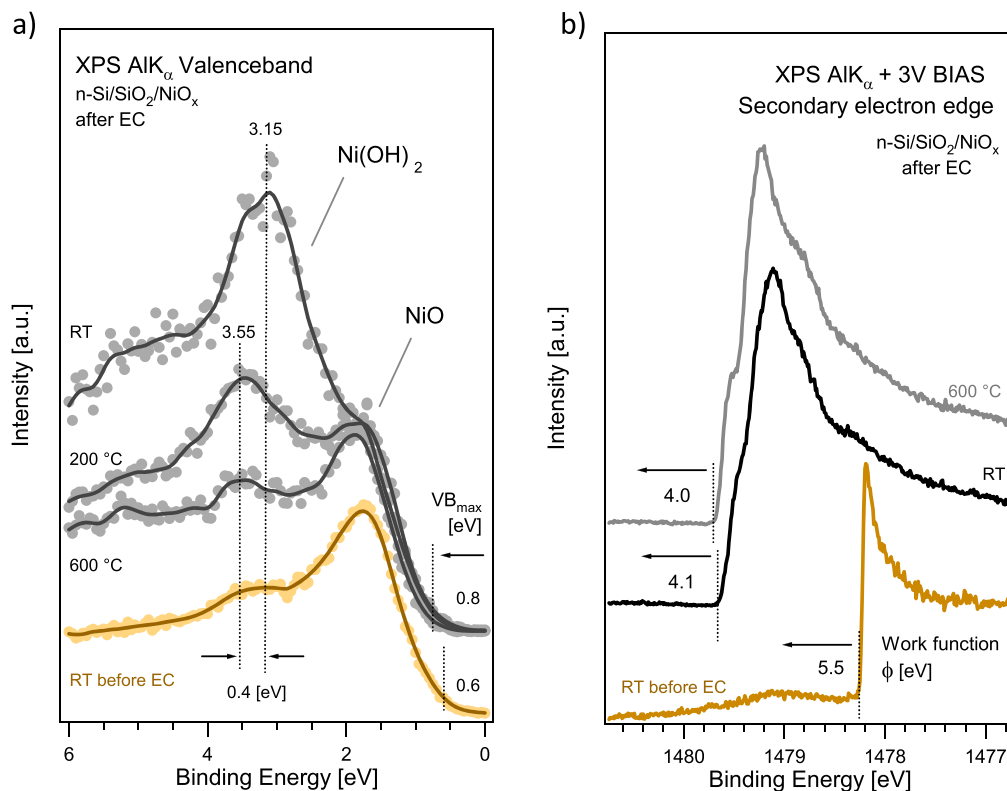


Figure 8. (a) Comparison of XPS valence band spectra of the n-Si/SiO₂/NiO_x photoanode sputtered at room temperature taken before and after the CV treatment. Additionally, the valence band spectra of the 200 °C, 400 °C, and 600 °C samples after EC are drawn in with the surface of the NiO_x thin films mainly consisting of a newly formed Ni(OH)₂ layer. The solid lines result from smoothing the experimental data by averaging over adjacent data points (five to each side). b) XPS measured secondary electron cut off edges of the RT sample recorded with an additional 3 V bias voltage before and after EC. The spectrum of the 600 °C sample after EC is included for comparison.

in Fig. 6 we find an emission at around 3.2 eV binding energy indicating the transformation of most likely Ni₂O₃ to Ni(OH)₂. We attribute this species to the OER reaction since height and thus concentration of the nickel hydroxide species is highest for the most efficient RT prepared NiO_x thin film. Moreover, secondary electron cut off edges of the RT sample before and after EC are pictured in Fig. 8b together with the spectrum of the 600 °C sample after EC. Obviously, the conditioning process upon the EC treatment leads to a distinctive change of the work function especially for the RT prepared sample with a value of $\Phi = 4.1$ eV. Regarding the 600 °C sample, a closer look to the secondary electron cut off unveils a step like behaviour which hints to an overlap of two slightly different materials consisting most probably of Ni(OH)₂ and NiOOH that are arranged on the newly formed surface side by side. This effect is less pronounced on the RT sample leading to the assumption that the surface is predominantly covered by the material that is better suited for the OER, namely Ni(OH)₂.

Based on the XP valence band spectra in Fig. 8, energy level diagrams of the RT sample before and after EC are depicted in Fig. 9. The valence band maximum shifts from 0.6 to 0.8 eV after the EC treatment while the position of the silicon valence band is assumed to be unchanged. In addition, the work function significantly changes from 5.5 to 4.1 eV which confirms the formation of a new h-NiO_x related surface phase. As a consequence, the resulting dipole drop over the whole n-Si/SiO_x/NiO_x device structure shifts from $\delta = 0.95$ to -0.45 eV with a pronounced change of sign. The Ni(OH)₂ related state is with 3.15 eV far below the topmost position of the silicon valence band at the n-Si/SiO_x interface which is located roughly 0.6 eV below the Fermi level. Thus, it is unclear how photo-generated holes participate in the OER related process by reaching these states. It is assumed that the Ni(OH)₂ emissions in the valence band spectra in Fig. 8a describe the final point of a dynamic reaction chain resulting in the evolution of oxygen which is not

accessible with the methods used in this work. The OER at the n-Si/SiO_x/NiO_x photo-anode under alkaline conditions in aqueous solution is by far more complex with respect to energy and time related issues. Apparently, the Ni(OH)₂ peaks shift with increasing deposition temperature from 3.15 eV towards 3.55 eV. Although a large error in the range of several hundred meV is expected due to averaging and normalization, the observed shift of 0.4 eV correlates with the shift of the OER onset potential in Fig. 5 which is nearly the same with about 0.35 V and which goes into the right direction.

Conclusions

Thin NiO_x layers were deposited on natively oxidized n-Si(100)/SiO_x substrates at different substrate temperatures of 600 °C, 400 °C, and 200 °C as well as RT during magnetron sputter deposition. The composition of the pristine samples was analyzed by lab- and synchrotron-based XPS prior to photo-assisted CV in an alkaline electrolyte. The onset potential of the OER improves from 1.55 to 1.1 eV (vs RHE) with decreasing deposition temperature. The XPS analysis of the pristine films shows that NiO_x consists of stoichiometric NiO and an oxygen rich NiO_x ($x > 1$) phase called in short “Ni₂O₃.” With decreasing deposition temperature, up to 23% “Ni₂O₃” is found in the sputtered NiO_x films. For the excitation energy dependent synchrotron measurements, the “Ni₂O₃”/NiO ratio decreases with increasing photon energy. However, the course of the “Ni₂O₃”/NiO ratio does not fit to a simple layer model for the structure of the NiO_x film, but can be explained by NiO grains that become larger with increasing temperature and by “Ni₂O₃” filled grain boundaries that become smaller in the probed information depth region ranging from 5 to 25 Å electron mean free path λ . In addition, a closed “Ni₂O₃” film as overlayer is postulated for the RT prepared sample. After CV under illumination hydrogenated h-NiO_x is formed which consists of NiOOH and Ni(OH)₂ while “Ni₂O₃”

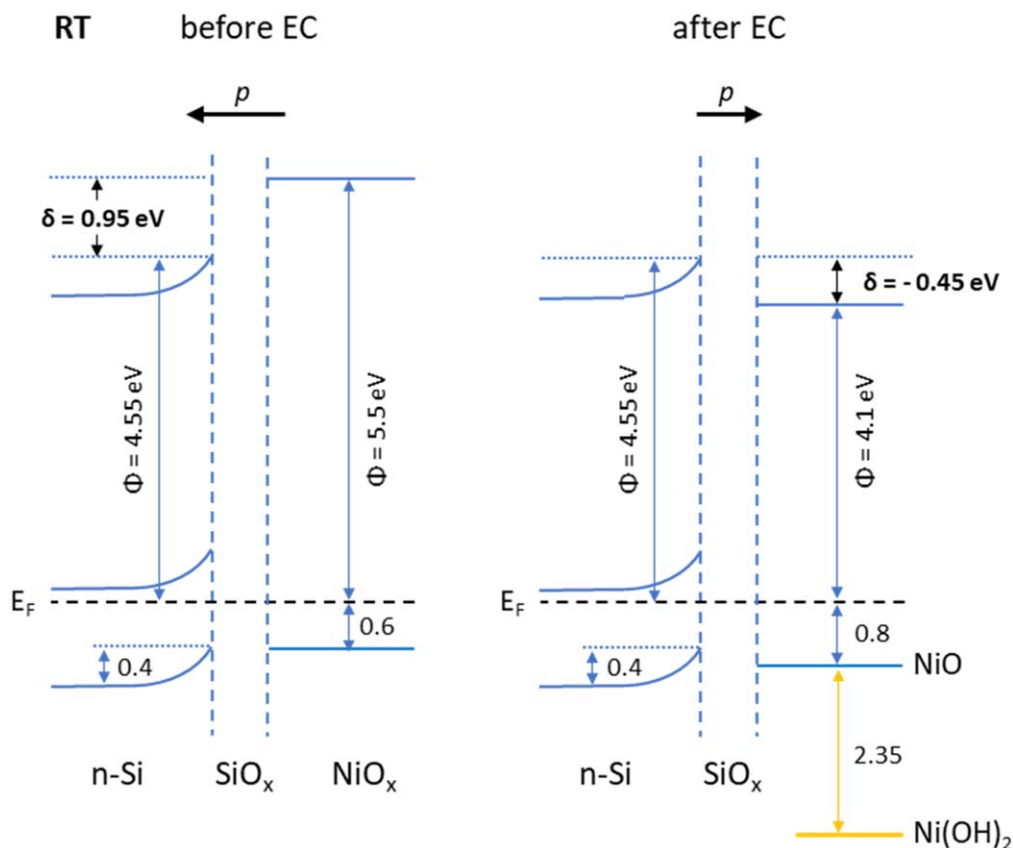


Figure 9. Energy level alignment of the n-Si/SiO₂/NiO_x photoanode sputtered at RT before and after EC as deduced from the valence band spectra in Fig. 8. Further details are discussed in the text.

disappeared. The h-NiO_x/NiO ratio also increases with decreasing deposition temperature. As the h-NiO_x content is larger than the “Ni₂O₃” content was for the pristine samples, hydroxylation reactions involving both, stoichiometric Ni₂O₃ and NiO are suggested according to $x\text{Ni}_2\text{O}_3 + y\text{NiO} + (y+x)\text{H}_2\text{O} \rightarrow y\text{Ni}(\text{OH})_2 + 2x\text{NiOOH}$. The impact of carbon contamination or incorporation of residual iron from the electrolyte was cut but not deepened as the collected data were not robust enough. Besides this, the investigations in this work reveal that mainly “Ni₂O₃” promotes the hydroxylation reaction which is beneficial for the OER reaction.

Acknowledgments

Financial support through the project “fundamentals of electrochemical phase boundaries at semiconductor/electrolyte interfaces” GEP-HE funded by the German Federal Ministry of Education and Research BMBF under contract 13XP5023A and by the European Union under the a-leaf project (732840-A-LEAF) is gratefully acknowledged. We thank HZB for the allocation of synchrotron radiation beamtime at the BESSY II UE56_2-PGM-1 beamline and for financial support.

ORCID

M. Fingerle <https://orcid.org/0000-0002-5416-7055>
 W. Calvet <https://orcid.org/0000-0002-1606-4645>
 W. Jaegermann <https://orcid.org/0000-0003-3677-4481>

References

- D. Cappus, C. Xu, D. Ehrlich Jr, B. D. A. V. Shamery, K. A. Kuhlbeck, and H. Freund, “H.-J., hydroxyl groups on oxide surfaces: NiO(100), NiO(111) and Cr₂O₃(111).” *Chem. Physics*, **177**, 533 (1993).
- J. M. McKay and V. E. Henrich, “Surface electronic structure of NiO: defect states, O₂ and H₂O interactions.” *Phys. Rev. B*, **32**, 6764 (1985).
- R. Poulain, A. Klein, and J. Proost, “Electrocatalytic properties of (100)-, (110)-, and (111)-Oriented NiO thin films toward the oxygen evolution reaction.” *J. Phys. Chem. C*, **122**, 22252 (2018).
- R. P. Furstenuau, G. McDougall, and M. A. Langell, “Initial stages of hydrogen reduction of NiO(100).” *Surf. Sci.*, **150**, 55 (1985).
- J. C. d. Jesus, J. Carrazza, P. Pereira, and F. Zaera, “Hydroxylation of NiO films: the effect of water and ion bombardment during the oxidation of nickel foils with O₂ under vacuum.” *Surf. Sci.*, **45-157**, 34 (1998).
- P. Reckers, M. Dimamay, J. Klett, S. Trost, K. Zilberberg, T. Riedl, B. A. Parkinson, J. Brötz, W. Jaegermann, and T. Mayer, “Deep and shallow TiO₂ gap states on cleaved anatase single crystal (101) surfaces, nanocrystalline anatase films, and ALD titania ante and post annealing.” *J. Phys. Chem. C*, **119**, 9890 (2015).
- J.-Y. Jung, J.-Y. Yu, S. Yoon, B. Yoo, and J.-H. Lee, “A photoelectrochemical device with dynamic interface energetics: understanding of structural and physical specificities and improvement of performance and stability.” *Adv. Sustainable Syst.*, **2**, 1800083 (2018).
- M. R. Nellist, F. A. L. Laskowski, F. Lin, T. J. Mills, and S. W. Boettcher, “Semiconductor-electrocatalyst interfaces: theory, experiment, and applications in photoelectrochemical water splitting.” *Acc. Chem. Res.*, **49**, 733 (2016).
- L. Trotochaud, T. J. Mil, and S. W. Boettcher, “An optocatalytic model for semiconductor-catalyst water-splitting photoelectrodes based on in situ optical measurements on operational catalysts.” *J. Phys. Chem. Lett.*, **4**, 931 (2013).
- M. W. Kanan and D. G. Nocera, “In situ formation of an oxygen-evolving catalyst in neutral water containing phosphate and Co²⁺.” *Science*, **321**, 1072 (2008).
- S. Tengeler, M. Fingerle, W. Calvet, C. Steinert, B. Kaiser, T. Mayer, and W. Jaegermann, “The impact of different Si surface terminations in the (001) n-Si/NiO_x heterojunction on the oxygen evolution reaction (OER) by XPS and electrochemical methods.” *J. Electrochem. Soc.*, **165**, H3122 (2018).
- A. F. Holleman, E. Wiberg, and N. Wiberg, *Lehrbuch der Anorganischen Chemie*. (de Gruyter, Berlin, New York) (2007).
- N. N. Greenwood and A. Earnshaw, *Chemistry of the Elements*. (Elsevier Butterworth-Heinemann, Amsterdam) (1997).
- M. T. Greiner, M. G. Helander, Z.-B. Wang, W.-M. Tang, and Z.-H. Lu, “Effects of processing conditions on the work function and energy-level alignment of NiO thin films.” *J. Phys. Chem. C*, **114**, 19777 (2010).
- K. S. Kim and N. Winograd, “X-ray photoelectron spectroscopic studies of nickel-oxygen surfaces using oxygen and argon ion-bombardment.” *Surf. Sci.*, **43**, 625 (1974).
- K. S. Kim and R. E. Davis, “Electron spectroscopy of the nickel-oxygen system.” *J. Electron Spec. & Rel. Phen.*, **1**, 251 (1972).

17. P. R. Norton, R. L. Tapping, and J. W. Goodale, "A photoemission study of the interaction of Ni(100), (110) and (111) surfaces with oxygen." *Surf. Sci.*, **65**, 13 (1977).
18. M. Casas-Cabanas, J. Canales-Vazquez, J. Rodriguez-Carvajal, and M. R. Palaci, "Deciphering the structural transformations during nickel oxyhydroxide electrode operation." *J. Am. Chem. Soc.*, **129**, 5840 (2007).
19. M. Casas-Cabanas, M. D. Radin, J. Kim, C. P. Grey, A. V. d. Ven, and M. R. Palacin, "The nickel battery positive electrode revisited: stability and structure of the β -NiOOH phase." *J. Mater. Chem. A*, **6**, 19256 (2018).
20. L. Guerlou-Demourgues, L. Fournès, and C. Delmas, "In situ ^{57}Fe Mössbauer spectroscopy study of the electrochemical behavior of an iron-substituted nickel hydroxide electrode." *J. Electrochem. Soc.*, **143**, 3083 (1996).
21. V. Fidelskya and M. C. Toroker, "The secret behind the success of doping nickel oxyhydroxide with iron." *Phys. Chem. Chem. Phys.*, **19**, 7491 (2017).
22. A. J. Tkalych, K. Yu, and E. A. Carter, "Structural and electronic features of β -Ni(OH)₂ and β -NiOOH from first principles." *J. Phys. Chem. C*, **119**, 24315 (2015).
23. H. Bode, K. Dehmelt, and J. Witte, "Zur Kenntnis der Nickelhydroxidelektrode - I. über das Nickel (II)-hydroxidhydrat." *Electrochim. Acta*, **11**, 1079 (1966).
24. A. Szytula, A. Murasik, and M. Balanda, "Neutron diffraction study of Ni(OH)₂." *Phys. Stat. Sol.*, **b**, 125 (1971).
25. C. Greaves and M. A. Thomas, "Refinement of the structure of deuterated nickel hydroxide, Ni(OH)₂ by powder neutron diffraction and evidence for structural disorder in samples with high surface area." *Acta Cryst.*, **B42**, 51 (1986).
26. D. S. Hall, D. J. Lockwood, C. Bock, and B. R. MacDougall, "Nickel hydroxides and related materials: a review of their structures, synthesis and properties." *Proc. R. Soc. A*, **471**, 65 (2015).
27. M. Wehrens-Dijksma and P. H. L. Notten, "Electrochemical quartz microbalance characterization of Ni(OH)₂-based thin film electrodes." *Electrochim. Acta*, **51**, 3609 (2006).
28. R. S. McEwen, "Higher nickel oxides." *J. Phys. Chem.*, **75**, 1782 (1971).
29. H. Yang, G. Gao, F. Teng, W. Liu, S. Chen, and Z. Ge, "Nickel hydroxide nanoflowers for a nonenzymatic electrochemical glucose sensor." *J. Electrochem. Soc.*, **161**, B216 (2014).
30. M. F. Lichterman et al., "Direct observation of the energetics at a semiconductor/liquid junction by operando X-ray photoelectron spectroscopy." *Energy Environ. Sci.*, **8**, 2409 (2015).
31. M. Fingerle, S. Tengeler, W. Calvet, T. Mayer, and W. Jaegermann, "Water interaction with sputter-deposited nickel oxide on N-Si photoanode: cryo photoelectron spectroscopy on adsorbed water in the frozen electrolyte approach." *J. Electrochem. Soc.*, **165**, H3148 (2018).
32. S. D. Chavhan, R. Hansson, L. K. E. Ericsson, P. Beyer, A. Hofmann, W. Brütting, A. Opitz, and E. Moons, "Low temperature processed NiO_x hole transport layers for efficient polymer solar cells." *Org. Electronics*, **44**, 59 (2017).
33. A. P. Grosvenor, M. C. Biesinger, R. S. C. Smart, and N. S. McIntyre, "New interpretations of XPS spectra of nickel metal and oxides." *Surf. Sci.*, **600**, 1771 (2006).
34. M. C. Biesinger, B. P. Payne, L. W. M. Lau, A. Gerson, and R. S. C. Smart, "X-ray photoelectron spectroscopic chemical state quantification of mixed nickelmetal, oxide and hydroxide systems." *Surf. Interface Anal.*, **41**, 324 (2009).
35. S. Oswald and W. Brückner, "XPS depth profile analysis of non-stoichiometric NiO films." *Surf. Interf. Anal.*, **36**, 17 (2004).
36. R. P. Gupta and S. K. Sen, "Calculation of multiplet structure of core p-vacancy levels." *Phys. Rev. B*, **10**, 71 (1974).
37. F. U. Hillebrecht, J. C. Fuggle, P. A. Bennett, Z. Zolnierrek, and C. Freiburg, "Electronic structure of Ni and Pd alloys. II. X-ray photoelectron core-level spectra." *Phys. Rev. B*, **27**, 2179 (1983).
38. M. Taguchi et al., "Revisiting the valence-band and core-level photoemission spectra of NiO." *Phys. Rev. Lett.*, **100**, 1 (2008).
39. B. P. Payne, M. C. Biesinger, and N. S. McIntyre, "Use of oxygen/nickel ratios in the XPS characterisation of oxide phases on nickel metal and nickel alloy surfaces." *J. Electron Spectroscopy and Related Phenomena*, **185**, 159 (2012).
40. S. Tougaard, "Quases-IMFP-TPP2M." *Software version 2.2* (QUASES-Tougaard Inc., Denmark) (1994).
41. H. Lüth, *Surfaces and interfaces of Solids*. (Springer, Berlin) (1993).
42. G. Hollinger and F. J. Himpsel, "Oxygen chemisorption and oxide formation on Si(111) and Si(100) surfaces." *J. Vac. Sci. Technol. A*, **1**, 640 (1982).
43. L. Trotochaud, J. K. Ranney, K. N. Williams, and S. W. Boettcher, "Solution-cast metal oxide thin film electrocatalysts for oxygen evolution." *J. Am. Chem. Soc.*, **134**, 17253 (2012).
44. B. P. Payne, M. C. Biesinger, and N. S. McIntyre, "The study of polycrystalline nickel metal oxidation by water vapour." *J. Electron Spec. & Rel. Phen.*, **175**, 55 (2009).
45. L. Trotochaud et al., "Water adsorption and dissociation on polycrystalline copper oxides: effects of environmental contamination and experimental protocol." *J. Phys. Chem. B*, **122**, 1000 (2018).
46. L. Trotochaud, S. L. Young, J. K. Ranney, and S. W. Boettcher, "Nickel-iron oxyhydroxide oxygen-evolution electrocatalysts: the role of intentional and incidental iron incorporation." *J. Am. Chem. Soc.*, **136**, 6744 (2014).
47. K. J. May, C. E. Carlton, K. A. Stoerzinger, M. Risch, J. Suntivich, Y.-L. Lee, A. Grimaud, and Y. Shao-Horn, "Influence of oxygen evolution during water oxidation on the surface of perovskite oxide catalysts." *J. Phys. Chem. Lett.*, **3**, 3264 (2012).
48. S. Klaus, M. W. Louie, L. Trotochaud, and A. T. Bell, "Role of catalyst preparation on the electrocatalytic activity of Ni_{1-x}Fe_xOOH for the oxygen evolution reaction." *J. Phys. Chem. C*, **119**, 18303 (2015).
49. M. S. Burke, M. G. Kast, L. Trotochaud, A. M. Smith, and S. W. Boettcher, "Cobalt-Iron (Oxy) hydroxide oxygen evolution electrocatalysts: the role of structure and composition on activity, stability, and mechanism." *J. Am. Chem. Soc.*, **137**, 3638 (2015).